



Article

Towards a Miniaturized 3D Receiver WPT System for Capsule Endoscopy

Sadeque Reza Khan *  and Marc P.Y. Desmulliez 

Institute of Sensors, Signals and Systems, School of Engineering and Physical Sciences, Heriot-Watt University, Edinburgh EH14 4AS, Scotland, UK

* Correspondence: srk5@hw.ac.uk; Tel.: +44-7770089372

Received: 29 July 2019; Accepted: 15 August 2019; Published: 17 August 2019



Abstract: The optimization, manufacturing, and performance characterization of a miniaturized 3D receiver (RX)-based wireless power transfer (WPT) system fed by a multi-transmitter (multi-TX) array is presented in this study for applications in capsule endoscopy (CE). The 200 mm outer diameter, 35 μm thick printed spiral TX coils of 2.8 g weight, is manufactured on a flexible substrate to enable bendability and portability of the transmitters by the patients. The 8.9 mm diameter—4.8 mm long, miniaturized 3D RX—includes a 4 mm diameter ferrite rod to increase power transfer efficiency (PTE) and is dimensionally compatible for insertion into current endoscopic capsules. The multi-TX is activated using a custom-made high-efficiency dual class-E power amplifier operated in subnominal condition. A resulting link and system PTE of 1% and 0.7%, respectively, inside a phantom tissue is demonstrated for the proposed 3D WPT system. The specific absorption rate (SAR) is simulated using the HFSSTM software (15.0) at 0.66 W/kg at 1 MHz operation frequency, which is below the IEEE guidelines for tissue safety. The maximum variation in temperature was also measured as 1.9 °C for the typical duration of the capsule's travel in the gastrointestinal tract to demonstrate the patients' tissues safety.

Keywords: 3D receiver; capsule endoscopy; phantom; power transfer efficiency; specific absorption rate

1. Introduction

Capsule endoscopes (CEs) are increasingly used for patients suffering from gastrointestinal (GI) disorders, as the relatively painless procedure allows early stage detection and diagnosis. Since the introduction of the first capsule in the late 1990s [1], increasingly complex systems have been proposed by the scientific community to achieve high-quality diagnostic yields. Subelements for these capsules range from electromechanical actuators for biopsy [2,3], nonwhite-light imaging sensors [4,5], actuators for locomotion [6], to electronic systems [7]. However, the lack of available small size batteries with sufficient capacity for continuous operation prevent their integration into today's CE [8,9]. Therefore, the most promising present alternative is the wireless power transfer (WPT) to the capsule from an external transmitter (TX) [10,11].

WPT technology has established itself as a promising candidate for complex medical implantable devices (MIDs), such as neurostimulators, pacemakers, or retinal implants [12–14]. Unlike fixed MIDs, endoscopic capsules travel through the gastrointestinal track. Therefore, it is essential to design a method whereby power can be satisfactorily delivered to the capsule irrespective of its location and position with respect to the TX. Moreover, the volume of a typical capsule—11 mm outer diameter by 26 mm length [15]—places severe constraints on the size of the embedded receiver (RX), leading to a low power transfer efficiency (PTE) for the resulting system.

Different misalignment insensitive RX coils configurations have been reported in the literature for an extensive range of WPT applications. In research of Jonah (et al.) [16] and Liu (et al.) [17], a strongly coupled magnetic resonance-based WPT method is illustrated for 3D power transfer coils whereby two and three orthogonal and circular loops are connected to each other to attenuate the angular misalignment effect. This architecture offers PTE in air of more than 60% at 41.5 MHz [16] and 40% at 80.2 MHz [17], respectively, for the whole range of RX coil angular positions. However, the 100 mm outer diameter of the TX and RX are inappropriate for MIDs, such as CE, due to the strict size restriction of the RX inside the human body. Furthermore, the high operation frequencies of the proposed systems could cause significant tissue heating for long durations of continuous operation as encountered in CE, requiring therefore experimental validation regarding human tissue safety. A 3D WPT system is presented with six and four TX and RX coils, respectively, positioned at different locations of a $46 \times 24 \times 20 \text{ cm}^3$ of a home cage of rodent and a box of $11 \times 20 \times 22 \text{ mm}^3$ installed on the head of a rat, respectively [18]. At 13.56 MHz operation frequency, PTEs of 23.6–33.3% and 6.7–10.1% have been demonstrated in air for a head height of 8 and 20 cm, respectively. This multiple TX coil-based WPT configuration is, however, exceptionally complex for CE applications. In addition, the proposed 3D RX is significantly (1.5 times) bigger than the typical volume of the capsules leaving therefore no room for sensing modalities. In research of Lenaerts (et al.) [19], a 3D receiver composed of three orthogonal coils stretched inside the 10 mm outer diameter, 13 mm length capsule, achieves a PTE of 1% in air at 1 MHz using a cylindrical TX coil of 41 and 30 cm in diameter and length, respectively, surrounding the patient. The specific absorption rate (SAR) recorded is 0.4 W/kg. In publication of Zhiwei (et al.) [20], a 3D WPT system is proposed for CE, whereby a ferrite slab is used to wind the RX coils around it. The 5% efficiency of the wireless link is measured for a 218 kHz frequency in air, with TX and RX coils of 400 mm and 11.5 mm diameters, respectively. The measured SAR of 8 W/kg is, however, well above the recommended IEEE guidelines regarding tissue safety [21]. A omnidirectional miniaturized RX coil analogous to that in research of Jonah (et al.) [16] and Liu (et al.) [17] is demonstrated in work of Pacini (et al.) [22] for CE WPT applications. However, a $24 \times 18 \text{ mm}^2$ size of the RX is not appropriate for typical CE capsules. A PTE link of 5% in air is, however, achieved for a 7 cm separation distance from a square TX coil of $78 \times 52 \text{ mm}^2$ at 6.78 MHz. In this paper, a 3D RX along with a flexible multi-TX WPT system is proposed. Compared to previously published studies, the proposed architecture offers a miniaturized 3D RX of 8.9 mm diameter and 4.8 mm length, that can be integrated into a typical endoscopic capsule. Furthermore, the proposed WPT system demonstrates a 1% WPT-link efficiency at a 10 cm separation distance and 1 MHz operating frequency inside a muscle phantom. The SAR of 0.66 W/kg confirms tissue safety of the proposed system. The designed flexible and portable TX coils of 200 mm diameter can be easily mounted onto a patient's body compared to the previously proposed TX coils for CE.

A 3D type RX is therefore proposed in this study to satisfy the requirements of tolerance to capsule misalignment, small size, moderate heat dissipation, and satisfactory PTE. The 3D RX coil is fully investigated using a set of analytical expressions and optimized via a nested multidimensional optimization algorithm presented in research of Khan (et al.) [23]. A multi-transmitter (TX) system is utilized in this work to achieve higher PTE for large TX–RX separation distances. A flexible substrate is used to manufacture the TX coils which can be conformed to the patient's body and allow easy portability. Tissue safety is simulated in terms of specific absorption rate (SAR) using ANSYS HFSSTM (15.0) and validated experimentally by measuring temperature variations using a tissue phantom.

2. Full Characterization of the 3D RX Coils System

Figure 1 shows the proposed 3D RX coils system with and without copper wires. The radius R_F and height h_F of a ferrite rod are included in the system's core to increase the magnetic flux developed within the space enclosed by the coils allowing thereby the enhancement of TX and RX coils' mutual coupling [24]. The diameter and thickness of the holder are 8.9 and 4.8 mm, respectively. The three

coils are defined as RX_x , RX_y , and RX_z . Each coil, of wire diameter w , is assumed to have N_l loops and N_t layers.

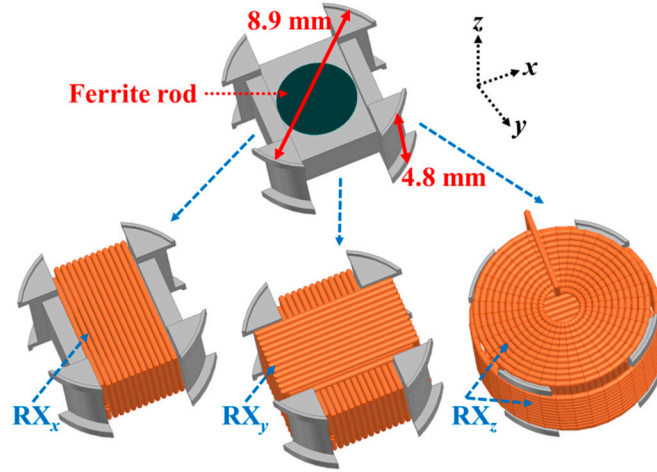


Figure 1. Coil holder architecture representation of the proposed 3D receiver (RX) coil.

2.1. Derivation of the Self-Inductance of the 3D RX Coil's Structure

The self-inductance, L_{self} , of each WPT coil (RX and TX) can be estimated as [25]:

$$L_{self} = \mu \sum_{i=1}^{N_l} R_i \left[\ln\left(\frac{16R_i}{w}\right) - 2 \right] + 2\mu \sum_{i=1}^{N_l} \sum_{j=1}^{N_l} \frac{\sqrt{R_i R_j}}{\alpha_{ij}} \left[\left(1 - \frac{\alpha_{ij}^2}{2}\right) K(\alpha_{ij}) - E(\alpha_{ij}) \right] \times (1 - \delta_{ij}) + 2\mu \sum_{i=1}^{(N_l-1)} \sum_{j=1}^{N_l} \sum_{k=1}^{N_l \times (N_l-i)} \frac{\sqrt{R_j R_k}}{\alpha_{ij}} \left[\left(1 - \frac{\alpha_{jk}^2}{2}\right) K(\alpha_{jk}) - E(\alpha_{jk}) \right] \quad (1)$$

with

$$\alpha_{ij} = 2 \sqrt{\frac{R_i R_j}{(R_i + R_j)^2 + d_{ij}^2}} \quad (2)$$

where $\delta_{ij} = 1$ for $i = j$; $\delta_{ij} = 0$, otherwise. Furthermore, μ is defined as the medium permeability and d_{ij} is the distance between two layers of loops radii R_i and R_j . The second term of Equation (1) refers to the case of different loops in the same layer, whereas, in the third term, R_k is the radius of a loop in different perfectly aligned layers. In Equation (1), the complete elliptic integrals of the first and second kind are presented as K and E , respectively. The coils are assumed to be wound as Archimedean spirals [25]. Considering the ferrite effect L_{self} is rewritten as [24]:

$$L_F = L_{self} \left[2 - \frac{R_F^2}{R^2} \left(1 - \frac{\mu_F}{1 + D_c(\mu_F - 1)} \right) \right] \quad (3)$$

where R , D_c , and μ_F are the outer radius of the coil, demagnetizing factor, and relative intrinsic permeability of the ferrite material, respectively. D_c is defined as [24]:

$$D_c = \frac{3.04\zeta^{-0.056} R_F^2}{h_F^2 e^3} \left[e - \tan^{-1} e \right], \quad e = \sqrt{1 - \zeta^2} \quad (4)$$

where $\zeta = h_F/2R_F$. The expression for D_c is only applicable for $\zeta < 1$.

Figure 2 demonstrates the calculated and simulated self-inductance values as a function of the total number of turns, $N_l \times N_t$, without (WOF) and with ferrite (WF), respectively. Simulations were carried out using the 3D electromagnetic (EM) solver ANSYS HFSS™. The maximum relative difference between the calculated and simulated results in the ferrite case was only 6% for $R_F = 2.5$ mm,

$h_F = 2$ mm, and $w = 0.3$ mm. Furthermore, the frequency of operation, f , was selected as 1 MHz. This frequency was chosen for tissue safety, it also offers cheaper electronic circuitry compared the ISM band of 6.78 MHz in order to demonstrate the concept presented here. It must be noted that the coil's R varies with respect to the number of N_t .

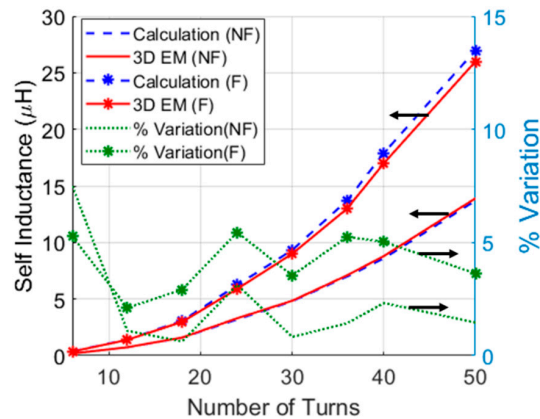


Figure 2. Self-inductance as a function of total number of turns, $N_t \times N_t$, without (NF) and with ferrite (F). The % variation between the analytical and 3D electromagnetic (EM) simulated results is illustrated on the vertical right axis. $R_F = 2.5$ mm, $h_F = 2$ mm, and $w = 0.3$ mm.

2.2. Derivation of the Mutual Inductance of the 3D RX Coil's Structure

The mutual inductance, M , of two current carrying loops, defined as C1 and C2 of respective radii R_{C1} and R_{C2} is proposed in research of Khan (et al.) [25] as:

$$M(R_{C1}, R_{C2}, d_r, \theta, \lambda) = \frac{\mu\pi R_{C1}^2 R_{C2}^2 \cos \theta \cos \lambda}{2(R_{C1}^2 + R_{C2}^2 + d_r^2 + d_2^2)^{\frac{3}{2}}} \times \begin{bmatrix} 1 + \frac{15}{64}(\Gamma_a^2 + 4\Gamma_b^2) + \frac{15}{64}(\Gamma_a^2 + 4\Gamma_c^2) \\ \cos^2 \theta \cos^2 \lambda + \frac{15}{8}\Gamma_d^2 (\sin \theta \cos \lambda \sin \lambda \cos \theta) \\ -\frac{15}{8}\Gamma_c\Gamma_d \cos \theta \cos \lambda (\sin \theta \cos \lambda + \sin \lambda \cos \theta) \\ -\frac{3}{2}(\delta_a - \delta_b(\tan \theta + \tan \lambda)) \end{bmatrix} \quad (5)$$

For a separation distance, d_r ; translational distance, d_2 ; roll and pitch rotational angle, θ and λ , respectively. The parameters $\Gamma_a, \Gamma_b, \Gamma_c, \Gamma_d$, and Γ_e are lesser than unity and explained in research of Khan (et al.) [25], together with δ_a and δ_b . Finally, the total mutual inductance, M_{total} , for T_{C1} layers and L_{C1} loops for coil C1 and T_{C2} layer and L_{C2} loops for coil C2 is written as [24,25]:

$$M_{total} = \sum_{i=1}^{T_{C1}} \sum_{j=1}^{T_{C2}} \sum_{k=1}^{L_{C1}} \sum_{l=1}^{L_{C2}} M \left(\begin{matrix} R_{C1:k}, R_{C2:l} \\ d_{r(i,j)}, d_2, \theta, \lambda \end{matrix} \right) \times \left[2 - \frac{R_F^2}{R^2} \left(1 - \frac{\mu_F}{1 + D_c(\mu_F - 1)} \right) \right] \quad (6)$$

where $R_{C1:k}$ and $R_{C1:l}$ are the radii of the k^{th} loop of C1 and l^{th} loop of C2, respectively. Furthermore, $d_r(i,j)$ is defined as [25]:

$$d_r = d_{r(N_{t,C1}, N_{t,C2})} = d_1 + [(N_{t,C1} - 1) \times (w_{C1} + s_{t,C1})] + [(N_{t,C2} - 1) \times (w_{C2} + s_{t,C2})] \quad (7)$$

where d_1 is the top and bottom layer's center-to-center distance of C1 and C2, respectively. Wire diameter and spacing between loops of a coil C_i are defined as w_{Ci} and $s_{t,Ci}$, respectively.

2.3. AC Resistance of the WPT Coil

The DC resistance, R_{DC} , is the significant part of the AC resistance of a WPT coil and calculated as [23,26,27]:

$$R_{DC} = \frac{8R\rho N_t l}{w^2} \tag{8}$$

where ρ is the copper wire resistivity and l is the length of the loops in one layer as defined in research of Khan (et al.) [23]. The AC resistance, R_{AC} , is the addition of skin and proximity effect resistors, R_{skin} and R_{prox} , respectively, and can be written as [28]:

$$R_{AC} = R_{skin} + R_{prox} \tag{9}$$

R_{skin} can be asymptotically represented as [29]:

$$R_{skin} = \frac{R_{DC}w^2}{4\delta(w - \delta)} \tag{10}$$

where δ is the skin depth [16–18]. In addition, R_{prox} , is defined as [30,31]:

$$R_{prox} = \frac{w^4}{32}\pi^3(\alpha\omega\mu)^2\sigma_c R I N_t \tag{11}$$

where σ_c is the conductivity of the copper and $\omega = 2\pi f$ is the radial operation frequency. The shape factor, α , is calculated as [30]:

$$\alpha = \sqrt{\frac{\sum_{i=1}^{N_l \times N_t} R_i \times H_i^2}{\sum_{i=1}^{N_l \times N_t} R_i \times I_i^2}} \tag{12}$$

where H_i and I_i are the intensity of the applied magnetic field and current flowing through to the i^{th} wire, respectively [32].

The simplified closed form alternative current (AC) resistance with the effect of ferrite on the copper wire in the 3D RX is provided in publication of Theilmann (et al.) [24], and estimated using the iterative EM simulation as:

$$R_F = R_{AC} \times \frac{\zeta R}{0.001\zeta^{-0.056}} \tag{13}$$

Taking the expression of R_{AC} of the printed spiral coil (PSC) in research of Khan (et al.) [23], and the same coils and ferrite dimensions, Figure 3 shows the analytical and 3D EM simulated AC resistance without (WOF) and with ferrite (WF) as a function of the total number of turns at $f = 1$ MHz.

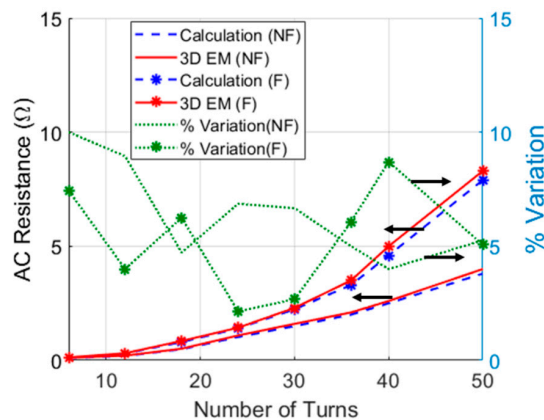


Figure 3. AC resistance presented as a function of total number of turns, $N_l \times N_t$, without (NF) and with ferrite (F). The % variation between calculation and 3D EM simulation is illustrated on the vertical right axis.

The maximum percentage of variation between the calculated and simulated results was less than 10%. The higher % variation at a lower number of turns is due to the very small value of resistance. The parasitic capacitance influence analysis of the copper wire and PSC are explained in research of Yang (et al.) [33] and Khan (et al.) [23], respectively.

3. Optimization of the Multi-TX and 3D RX System

A concept diagram of multi-TX and 3D RX WPT systems is presented in Figure 4, where $k_{i,j} = (M_{ij} / \sqrt{L_i L_j})$ is the coupling coefficient between coils C_i and C_j [11,26,27]. The TX coils are externally powered with the driving sources $F_1(t)$ and $F_2(t)$. In this case, only the z-axis of the 3D RX coil is considered. The RX coil output is associated with the load resistance, R_L . Moreover, the coupling rate between coils C_i and C_j is defined as $K_{ij} (\approx K_{ji})$. The multi-TX system can be illustrated by using the coupled-mode theory as [34,35]:

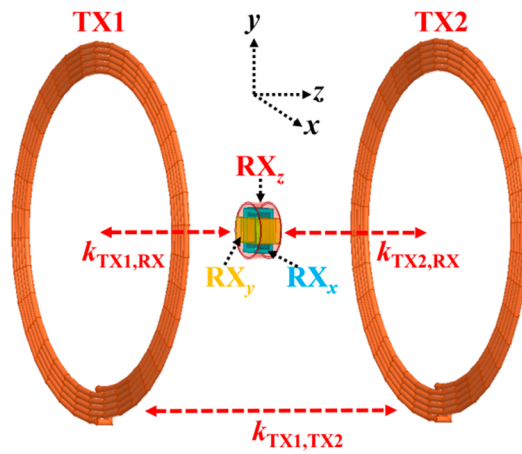


Figure 4. Concept diagram of the multi-transmitter (multi-TX) and 3D RX wireless power transfer (WPT) system.

$$\Gamma_{TX1} A_{TX1} - jK_{TX1,TX2} A_{TX2} - jK_{TX1,RX} A_{RX} = 0 \tag{14}$$

$$\Gamma_{TX2} A_{TX2} - jK_{TX2,TX1} A_{TX1} - jK_{TX2,RX} A_{RX} = 0 \tag{15}$$

$$(\Gamma_{RX} + \Gamma_L) A_{RX} - jK_{RX,TX1} A_{TX1} - jK_{RX,TX2} A_{TX2} = 0 \tag{16}$$

where Γ_i is the resonance width or rate of intrinsic decay of transmitter TX_i , receiver RX , or load L , due to the object absorption and radiation losses. The field amplitude inside a coil is $a_i(t) = A_i \cdot e^{-j\omega t}$. Considering $K_{TX1,TX2}$ to be negligible due to the large distance between $TX1$ and $TX2$, A_{TX1}/A_{RX} and A_{TX2}/A_{RX} can then be written as:

$$\frac{A_{TX1}}{A_{RX}} = \frac{K_{TX1,RX}(\Gamma_{RX} + \Gamma_L)\Gamma_{TX2}}{(jK_{TX1,RX}^2 \Gamma_{TX2} + jK_{TX2,RX}^2 \Gamma_{TX1})} \tag{17}$$

$$\frac{A_{TX2}}{A_{RX}} = \frac{K_{TX2,RX}(\Gamma_{RX} + \Gamma_L)\Gamma_{TX1}}{(jK_{TX1,RX}^2 \Gamma_{TX2} + jK_{TX2,RX}^2 \Gamma_{TX1})} \tag{18}$$

The power at coil i can be defined as $P_i = 2\Gamma_i |A_i|^2$. The total power delivered to the system from the source is $P_{TOT} = P_{TX1} + P_{TX2} + P_{RX} + P_L$. The power transfer efficiency, PTE, of the system, η defined as the ratio between the power delivered to the load and the total power delivered, is therefore:

$$\eta = \frac{P_L}{P_{TOT}} = \frac{1}{2 + \frac{\Gamma_{RX}}{\Gamma_L} \left[2 + \frac{\Gamma_{TX1}}{\Gamma_{RX}} \left| \frac{A_{TX1}}{A_{RX}} \right|^2 + \frac{\Gamma_{TX2}}{\Gamma_{RX}} \left| \frac{A_{TX2}}{A_{RX}} \right|^2 \right]} \tag{19}$$

or

$$\eta = \frac{1}{2 + \frac{Q_L}{Q_{RX}} \left[2 + \frac{1}{\text{FOMD}^2} \left(1 + \frac{Q_{RX}}{Q_L} \right)^2 \right]} \quad (20)$$

where Q_{RX} and $Q_L (= 2\pi f \cdot L_{RX}/R_L)$ are the quality factor of the RX coil and load, respectively. L_{RX} is the inductance of the coils. The distance dependent figure of merit (FOMD) is defined as:

$$\text{FOMD} = \sqrt{k_{TX1,RX}^2 Q_{TX1} Q_{RX} + k_{TX2,RX}^2 Q_{TX2} Q_{RX}} \quad (21)$$

where Q_{TX1} and Q_{TX2} are the Q-factors of the TX1 and TX2 coils. Expression for the optimized load, R_L^* is:

$$R_L^* = \frac{2\pi f L_{RX} \sqrt{1 + 2\text{FOM}^2}}{Q_{RX}} \quad (22)$$

Total PTE for the two TX and RX 3D WPT systems is then defined as:

$$\eta_{\text{total}} = \eta_{RX}(x\text{-axis}) + \eta_{RX}(y\text{-axis}) + \eta_{RX}(z\text{-axis}) \quad (23)$$

A nested multi-dimensional optimization algorithm presented in research of Khan (et al.) [23] is adopted to optimize the proposed multi-TX and 3D RX WPT systems using Equations (1)–(23). This algorithm extracts coil parameters such as wire width and number of turns to achieve maximum WL-PTE. The complete optimization routine requires approximately 20 min for the Intel (R) Xeon (R) CPU E5-2640 with processor speed of 2.5 GHz and 128 GB of RAM (HP Z820 workstation). The optimized load, R_L^* , is calculated as 6.5 Ω for $d_r = 10$ cm. The optimized coil parameters of TX and 3D RX are listed in Table 1, where s and N are the spacing between two copper wires and total number of turns, respectively.

Table 1. Optimized transmitter (TX) and receiver (RX) coil parameters.

Parameter	R (mm)	w (mm)	s (mm)	N	L_F (μH)	Q
TX	101	2.5	2	14	30	88
RX (x-, y- and z-axis)	4.45	0.2	-	35	8.3	33.5

4. Experimental Setup

3D printed coil holders without and with a ferrite rod are proposed as 3D RX demonstrators (Figure 5). 3D printing of the coil holder was carried out using Vero white material produced by Stratasys (Eden Prairie, Minnesota, United States) and an Object500 Connex printer. The outer diameter of the coil holder without the ferrite, Figure 5a, is 8.9 mm. The material 61 Nickel Zinc (NiZn) ferrite rod of height $h_F = 2$ mm and radius $R_F = 2$ and 2.5 mm, shown in Figure 5b,c, respectively, was adopted to improve the PTE of the 3D WPT system for the same outer diameter of the holder. The outer diameter and thickness of the proposed 3D RX and its copper wire winding were 8.9 and 4.8 mm, respectively.

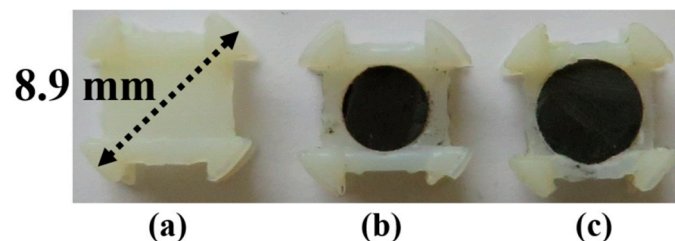


Figure 5. Manufactured coil holders. (a) Without ferrite. (b) With 4 mm diameter ferrite. (c) With 5 mm diameter ferrite.

The complete experimental setup with the multi-TX coils and 18 cm diameter spherical phantom is presented in Figure 6. The optimized parameters presented in Table 1 were used to fabricate the TX and RX coils. The TX coils are manufactured on a DuPont™ Pylux AP flexible substrate of 150 μm thickness with a 35 μm thick copper cladding. The TX coils were placed 1 cm away from the outer surface of the phantom globe, resulting in a total distance of 20 cm between the RX. The TX coils were driven by separate TX circuits (class-E amplifier) fabricated on a single circuit board labeled TX circuit in Figure 6. The phantom with similar electrical properties as human muscle tissue was prepared using hydrophilic organic powder and degassed water [7]. A RX circuit test bench with variable capacitors to adjust resonant conditions of the RX coils and optimize load resistors was used to measure the total WL-PTE as defined in Equation (23). The Schottky diode-based bridge rectifier for each RX coil was also embedded in the RX circuit to measure the complete system efficiency. PTE was measured using a Keysight technologies current probe (1147B) and oscilloscope. The Q-factors of the TX and RX coils at different frequencies were measured using the impedance analyzer HP 4192A. Temperature variation inside the phantom globe was measured by a Microcontroller Arduino Nano 3.0, using a serial communication window.

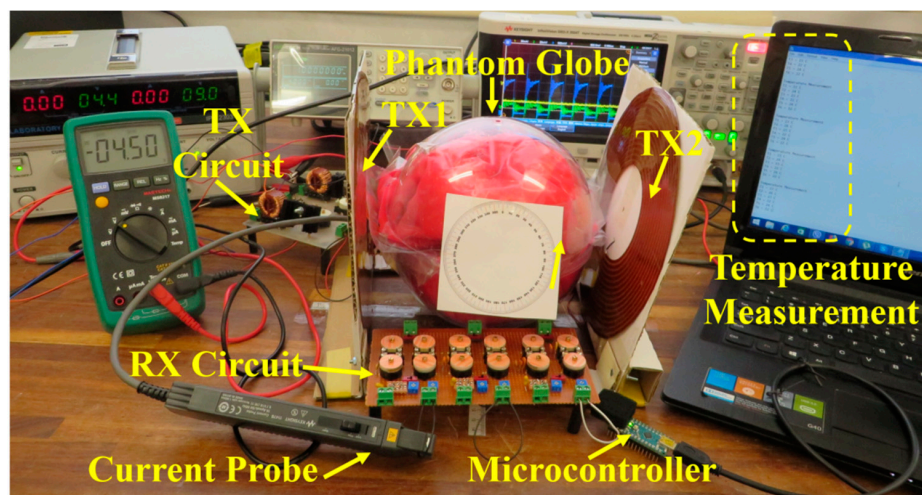


Figure 6. Full experimental setup.

Figure 7 shows the cross-section of the phantom globe, which is made of two identical hemispheres filled with the phantom tissues described above. The 3D RX coil was mounted at the center, and five temperature sensors (TSs) were inserted approximately equidistantly around the RX coil. A sixth thermistor, TS6, was placed outside the phantom to measure room temperature.

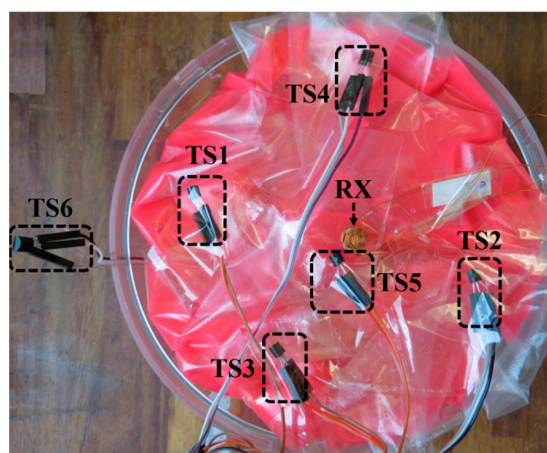


Figure 7. 3D RX coil and temperature sensor installation inside the phantom.

5. Results and Discussion

Variations in frequency of the theoretical, simulated, and measured values of the Q-factors for TX and RX coils are presented in Figures 8 and 9, respectively. For the RX coil, the three axes are shown for the frequency range of 500 kHz to 5 MHz. For each frequency, the ideal load, R_L^* was calculated. Excellent agreement was recorded between calculated, simulated, and measured values for both figures.

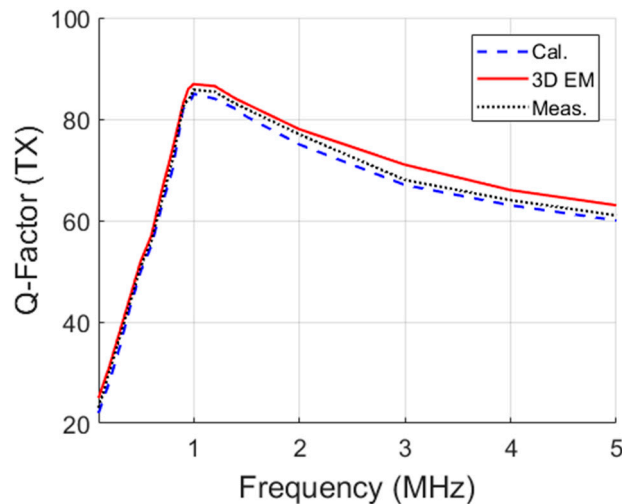


Figure 8. TX coil Q-factor with frequency.

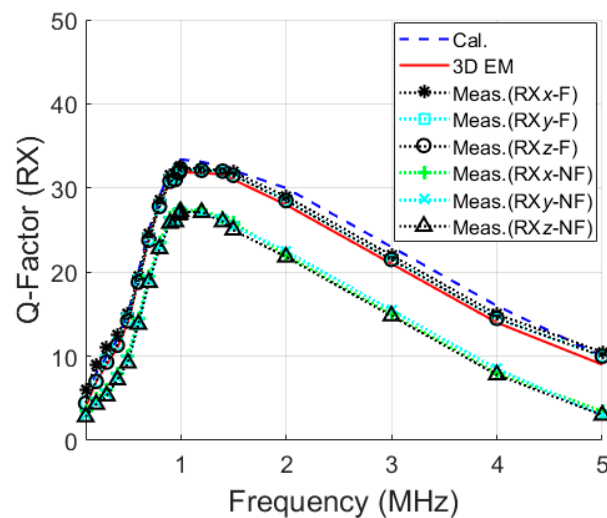


Figure 9. RX coil Q-factor with frequency.

Variations in Q-factors for RX coils with (F) and without (NF) ferrite rods are displayed in Figure 9. The highest Q-factor was achieved at around 1 MHz.

PTE variations are shown in Figure 10 for a separation distance between TX and RX ranging from 0.5 to 20 cm. PTEs for both single and multi-TX coils are recorded in air and phantom. A high PTE was recorded for a single-TX coil at a small distance compared to multi-TX. A significant drop in the PTE after 8 cm was noticed with PTE becoming negligible at 20 cm. In contrast, the multi-TX coils demonstrate promising PTE in the 5–15 cm distance, which is the location of the GI tract in an average human body. The measured PTEs for the 10 cm distance of 3D RX with ferrite rod ($R_F = 2$ mm) from a single TX coil in air and phantom were 0.9 and 0.75%, respectively. Increased PTE at 1.3 and 1% was achieved for a multi-TX WPT system in air and phantom, respectively. No significant difference

was observed in air or in the phantom due to the low absorption of the phantom tissue at 1 MHz. Furthermore, the measured PTE for the 3D RX without ferrite rod (NF) and multi-TX was 0.8% at 10 cm distance in air. A similar WPTE was achieved for 3D RX with $R_F = 2.5$ mm and the multi-TX WPT system.

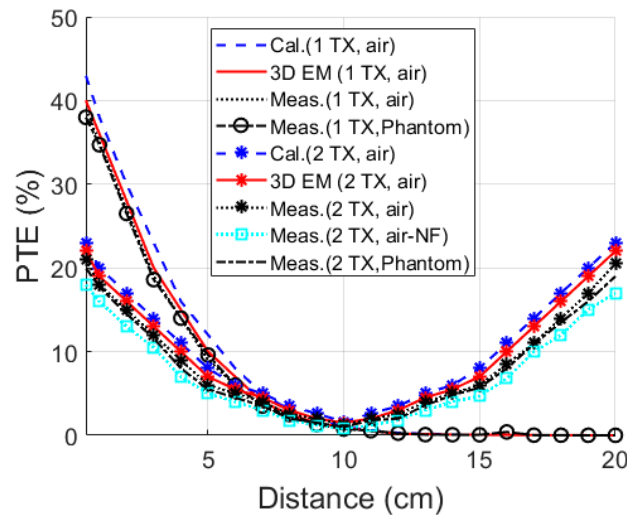


Figure 10. Power transfer efficiency (PTE) of the link as a function of separation distance between TX and RX at 1 MHz operation frequency.

The total measured PTE as shown in Equation (23), is shown in Figure 11 for angular rotation of 0° to 90° for the phantom globe in the x -, y -, and z -axes. The WPT system maintains total PTE over 0.9% for complete rotation of the 3D RX inside the phantom validating, thereby the significant robustness of the proposed WPT system against the angular movement of the capsule inside the GI tract. The translational misalignment from -7 cm (left) to $+7$ cm (right), shown in Figure 12, indicates a minimum measured WL-PTE of 0.84% in air and 0.7% in the phantom.

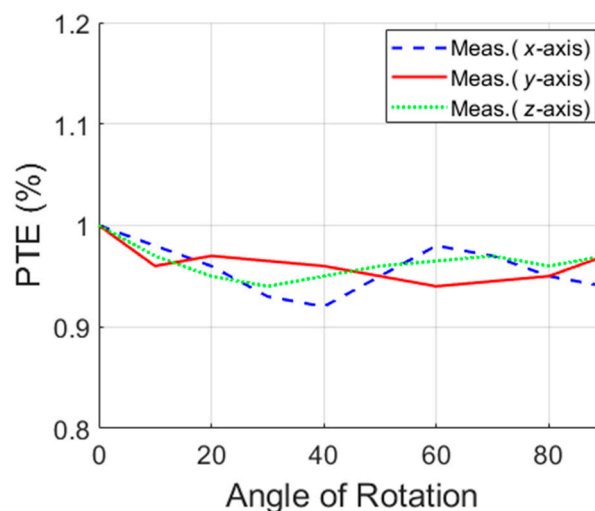


Figure 11. PTE versus angular rotation in different axis.

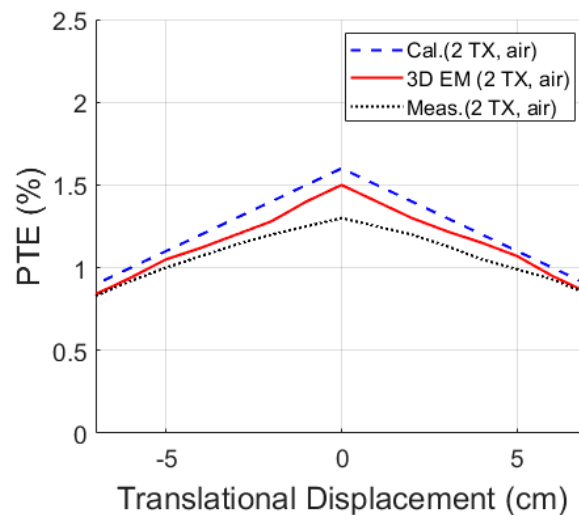


Figure 12. PTE versus translational displacement ($d_r = 10$ cm).

SAR simulation results using the ANSYS HFSS™ human model at 1 MHz and 6.78 MHz (ISM band) are shown in Figures 13 and 14, respectively, for 10 W of input power. The SAR obtained at 1 MHz, 0.66 W/kg, is lower than the IEEE standard of 2 W/kg for 10 g of tissue [21]. However, the SAR was recorded at 1.54 W/kg for 6.78 MHz of operation frequency, which is significantly closer to the IEEE standard of tissue safety.

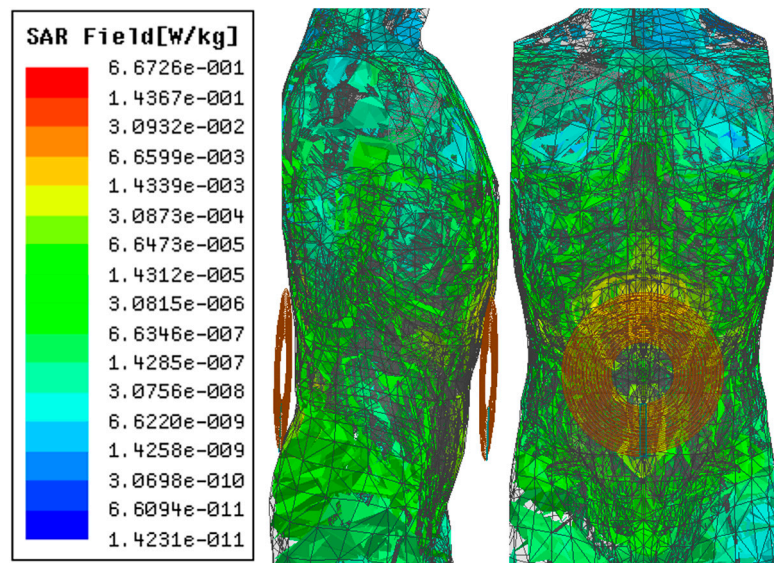


Figure 13. Specific absorption rate (SAR) simulation in a human model in ANSYS HFSS ($f = 1$ MHz).

Temperature rise inside the tissue was also measured in the phantom using multiple TSs for a typical capsule transit time of 10-hour inside the GI tract, shown as Figure 15.

The maximum temperature variation in the body (TS5) was 1.9 °C for a variation of 1.4 °C of room temperature (TS6). Temperature rise measurement in and around the capsule should also account for the additional temperature rise generated by the electronic processing inside the capsule to implement the requested sensing modalities as reported in research of Faerber (et al.) [7] and Lay (et al.) [36].

The figure of merit, *FOM*,

$$FOM = \frac{PTE \times \text{separation distance} \times \text{axes}}{TX \text{ diameter} \times RX \text{ size} \times f \times SAR^2} \tag{24}$$

proposed in research of Khan (et al.) [37], is adopted here to compare the performance of the various WPT systems for CE with the proposed work. A higher FOM represents better WPT performance. In Equation (24), the term “axes” represents the many directions where the RX can receive power, which is three in our work. Results are presented in Table 2.

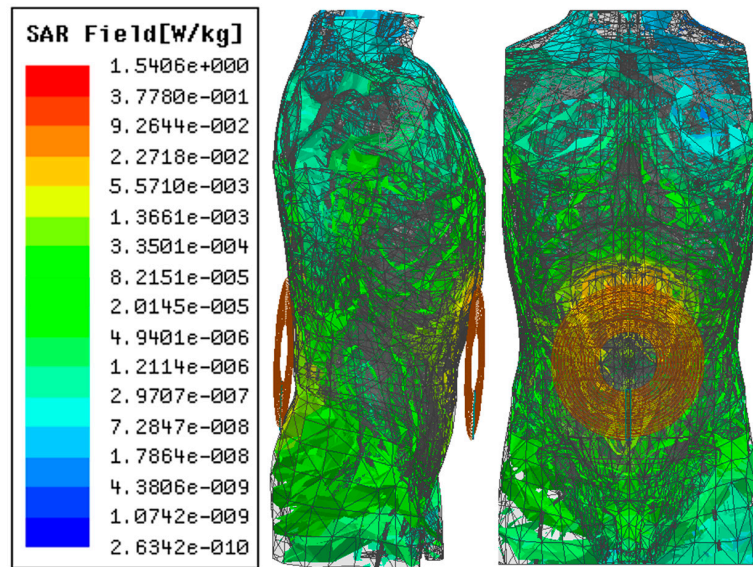


Figure 14. SAR simulation in a human model in ANSYS HFSS ($f = 6.78$ MHz).

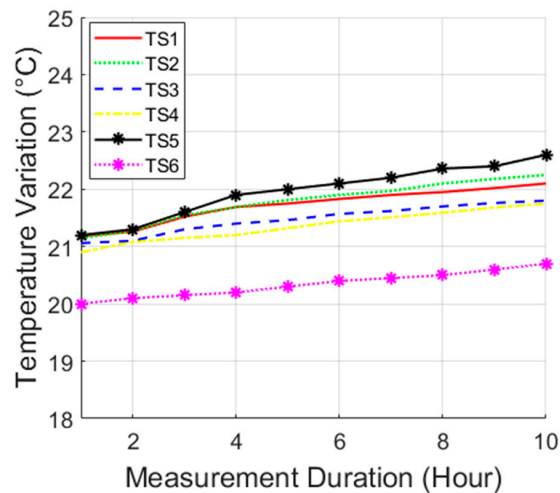


Figure 15. Variation of temperature in the complete capsule endoscopy (CE) duration.

Table 2. Performance comparison.

Parameter	[20]	[38]	[39]	[37]	This Work
TX Diameter (mm)	400	220	23.5	200	200
RX size (mm ²)	11.5 × 11.5	9 × 6	15 × 7	8 × 8	8.9 × 4.8
Axes (D)	3	1	1	3	3
Distance (cm)	20	7	5	10	10
WL-PTE (%)	5.02	0.7	1.21	1.3	1
f (MHz)	0.218	16.47	433.9	5	1
SAR (W/kg)	8	1.74	2.54	0.86	0.66
Test environment	Air	Pig muscle	Duck intestine	Muscle phantom	Muscle phantom
FOM ($\times 10^{-3}$) (25)	4.08	0.0824	0.009	8.23	80

WL-PTE: Wireless link power transfer efficiency. SAR: Specific absorption rate. FOM: Figure of merit.

In research of Zhiwei (et al.) [20], the proposed 3D WPT system achieved PTE of ~5% in air at 218 kHz frequency for a nonportable TX coil and higher SAR than recommended by the IEEE guidelines [21]. The WPT systems presented in research of Na (et al.) [38] and Ding (et al.) [39] are either sensitive to misalignment or display a high SAR [39]. The recent 3D WPT system presented in publication of Khan (et al.) [37] demonstrates promising PTE and SAR for CE application. The RX size ($8 \times 8 \text{ mm}^2$) is appropriate for typical CE. In this study, the proposed 3D RX coil is, however, smaller in size compared to previous works and offers therefore more space for other electronic processing circuitry or sensing modalities. However, PTE is lower compared to some previous works.

The complete WPT system with its electronic processing is presented in Figure 16, alongside analysis of the complete system efficiency (CSE). Two separate TX circuits were used to supply power to the multi-TX WPT system using a single signal generator. It is necessary to use same signal generator for both the TX coils to maintain the excitation with signals having the same phase. Phase variation would otherwise reduce drastically the PTE of the proposed system. A DC-fed energy injection single-ended class-E power amplifier (PA) was adopted for the unit TX circuit [40]. The closed-form equations of the subnominal model presented in research of Liu (et al.) [41] was utilized to design the PA at 1 MHz operating frequency. The IRF640 N-channel metal oxide field effect transistor (MOSFET) and EL7457 noninverting MOSFET driver in between signal generator and MOSFET were used to implement the PA.

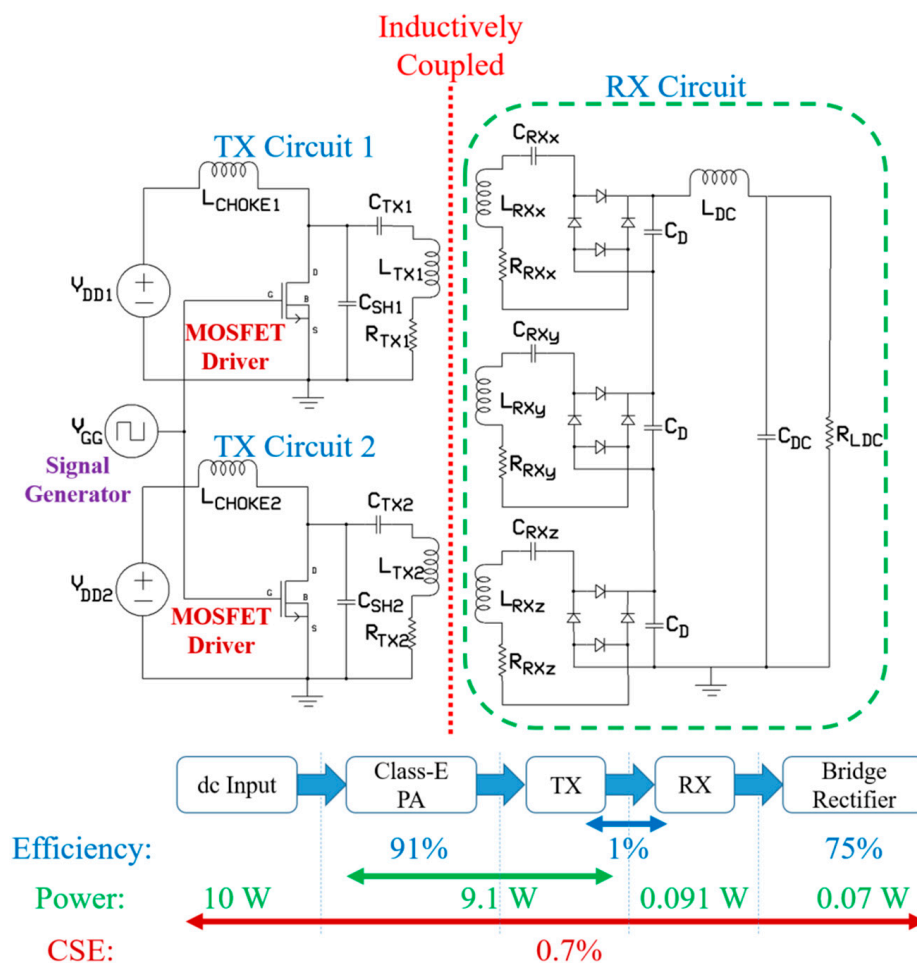


Figure 16. Efficiency of the complete WPT system and efficiency analysis.

Adjustable capacitors were used as shunt capacitors, $C_{SH} = 7 \text{ nF}$, and series resonant capacitors, $C_{TX} = 894 \text{ pF}$, for both TX circuits. The parasitic capacitance (400 pF according to the datasheet) of the

MOSFET was also included in C_{SH} . A radio frequency choke (RFC) inductor, $L_{CHOKE} = 10$ mH, was used to stabilize the output current of the TX circuits. The measured efficiency of the designed PA was 91% at 1 MHz, where L_{TX} and R_{TX} are the inductance and resistance of the TX coil, respectively. The inductively coupled RX circuit consists of three LC series resonant circuits formed by three RX coils and their resonant capacitors, C_{RX} . L_{RX} and R_{RX} are the inductance and resistance of the proposed 3D RX. Three full wave bridge rectifiers built with the Schottky diode DB2S20500L and surface mount package of dimensions $1.6 \times 0.8 \times 0.6$ mm³, were connected in a series rectification topology. The three outputs were then DC-combined and shared the same DC filter where $C_D = 100$ pF, $L_{DC} = 500$ nH [42] and $C_{DC} = 1$ μ F with the same value of the load resistor, R_{LDC} , considered in the PTE optimization.

The CSE of the WPT system was 0.7% with the PA, multi-TX WPT link, and Shottky diode-based bridge rectifier displaying respective efficiencies of 91%, 1%, and 75%. For a total input power of 10 W, i.e., input of 5 W for unit TX circuit, an output power of 70 mW is achieved which is higher than current commercial CE [43,44]. The proposed system can supply approximately 50 mW of power inside the phantom in the worst cases of angular and translational misalignment. It is possible to increase the output power of the proposed system by improving the efficiency of the class-E amplifier. In research of Liu (et al.) [41], the propose class-E amplifier can achieve maximum efficiency of 99.3% for an input signal duty ratio of 0.097. This can lead to an output power of 75 mW for the proposed WPT system in this paper. It should be possible to improve the CSE to 0.8% by utilizing high efficiency (more than 87%) rectifier circuits based application specific integrated chip (ASIC) [45,46]. Furthermore, the utilization of the modern 3D printing technology can lead to a more methodological manufacturing technique for the miniaturized 3D RX coil. Compared to the hand wound RX coil this technique can provide more space for layers and turns in the 3D RX and improve the overall PTE and CSE of the system.

6. Conclusions

In this paper, a 3D RX coil and multi-TX-based WPT system are presented for CE application. The WPT system operated at 1 MHz demonstrates a CSE of 0.7% at 10 cm separation distance inside the phantom. The proposed 8.9 mm diameter and 4.8 mm thick RX coil can easily fit into a standard endoscopic capsule. The measured results demonstrate promising PTE at larger separation distance and complete capsule rotation inside phantom. Implementing the TX coils using flexible substrate facilitates easy mounting of the transmitter and portability. Tissue safety is verified by simulating SAR and measuring temperature variations inside a tissue phantom. The proposed 3D WPT system is shown, therefore, to be a potential candidate as an alternative power source for CE.

Author Contributions: Conceptualization, S.R.K. and M.P.Y.D.; Methodology, S.R.K.; Software, S.R.K.; Validation, S.R.K.; Formal Analysis, S.R.K.; Investigation, S.R.K.; Resources, M.P.Y.D.; Data Curation, S.R.K.; Writing-Original Draft Preparation, S.R.K.; Writing-Review & Editing, M.P.Y.D.; Visualization, M.P.Y.D.; Supervision, M.P.Y.D.; Project Administration, M.P.Y.D.; Funding Acquisition, M.P.Y.D.

Funding: The authors of this article would like to acknowledge the financial support from the UK Engineering & Physical Sciences Research Council (EPSRC) through the programme grant entitled *Sonopill* (EP/K034537/2). Financial contribution from Heriot-Watt University, under the International Doctoral Training Account (DTA), is also gratefully acknowledged by Mr. Sadeque Reza Khan.

Conflicts of Interest: The authors declare no conflict of interest. The funders had no role in the design of the study; in the collection, analyses, or interpretation of data; in the writing of the manuscript, or in the decision to publish the results.

References

1. Iddan, G.; Meron, G.; Glukhovskiy, A.; Swain, P. Wireless capsule endoscopy. *Nature* **2000**, *405*, 417. [[CrossRef](#)] [[PubMed](#)]
2. Kong, K.C.; Cha, J.; Jeon, D.; Cho, D.I.D. A rotational micro biopsy device for the capsule endoscope. In Proceedings of the 2005 IEEE/RSJ International Conference on Intelligent Robots and Systems, Edmonton, AB, Canada, 2–6 August 2005; pp. 1839–1843.

3. Park, S.; Koo, K.-I.; Kim, G.-S.; Bang, S.M.; Song, S.Y.; Byun, J.-W.; Chu, C.-N.; Cho, D. “Dan” A Novel Micro-Biopsy Actuator for Capsular Endoscope using LIGA Process. In Proceedings of the TRANSDUCERS 2007-2007 International Solid-State Sensors, Actuators and Microsystems Conference, Lyon, France, 10–14 June 2007; pp. 209–212.
4. Shao, Q.; Liu, H.; Li, H.; Yang, Y. Miniature pH sensor for capsule endoscopy with composite diagnosis. In Proceedings of the IEEE SENSORS 2014 Proceedings, Valencia, Spain, 2–5 November 2014; pp. 339–342.
5. Cummins, G.; Cox, B.F.; Ciuti, G.; Anbarasan, T.; Desmulliez, M.P.Y.; Cochran, S.; Steele, R.; Plevris, J.N.; Koulaouzidis, A. Gastrointestinal diagnosis using non-white light imaging capsule endoscopy. *Nat. Rev. Gastroenterol. Hepatol.* **2019**, *16*, 429–447. [[CrossRef](#)] [[PubMed](#)]
6. Sungwook Yang, S.; Kitae Park, K.; Jinseok Kim, J.; Tae Song Kim, T.S.; Il-Joo Cho, I.-J.; Eui-Sung Yoon, E.-S. Autonomous locomotion of capsule endoscope in gastrointestinal tract. In Proceedings of the 2011 Annual International Conference of the IEEE Engineering in Medicine and Biology Society, Boston, MA, USA, 30 August–3 September 2011; Volume 2011, pp. 6659–6663.
7. Faerber, J.; Cummins, G.; Pavuluri, S.K.; Record, P.; Rodriguez, A.R.A.; Lay, H.S.; McPhillips, R.; Cox, B.F.; Connor, C.; Gregson, R.; et al. In Vivo Characterization of a Wireless Telemetry Module for a Capsule Endoscopy System Utilizing a Conformal Antenna. *IEEE Trans. Biomed. Circuits Syst.* **2017**, *12*, 95–105. [[CrossRef](#)] [[PubMed](#)]
8. Carta, R.; Sfakiotakis, M.; Pateromichelakis, N.; Thoné, J.; Tsakiris, D.P.; Puers, R. A multi-coil inductive powering system for an endoscopic capsule with vibratory actuation. *Sens. Actuators A Phys.* **2011**, *172*, 253–258. [[CrossRef](#)]
9. Bingquan, Z.; Guozheng, Y.; Zhiwei, J.; Yu, S. Portable Wireless Power Transmission System of a Video Capsule Endoscopy: Design and Realization. In Proceedings of the 2012 International Conference on Biomedical Engineering and Biotechnology, Macao, China, 28–30 May 2012; pp. 409–412.
10. Reza Khan, S.; Choi, G. Optimization of planar strongly coupled wireless power transfer system for biomedical applications. *Microw. Opt. Technol. Lett.* **2016**, *58*, 1861–1866. [[CrossRef](#)]
11. Khan, S.R.; Choi, G.S. Analysis and optimization of four-coil planar magnetically coupled printed spiral resonators. *Sensors (Switzerland)* **2016**, *16*, 1219. [[CrossRef](#)] [[PubMed](#)]
12. Silay, K.M.; Dehollain, C.; Declercq, M. A Closed-Loop Remote Powering Link for Wireless Cortical Implants. *IEEE Sens. J.* **2013**, *13*, 3226–3235. [[CrossRef](#)]
13. Zhang, X.; Ho, S.L.; Fu, W.N. A Hybrid Optimal Design Strategy of Wireless Magnetic-Resonant Charger for Deep Brain Stimulation Devices. *IEEE Trans. Magn.* **2013**, *49*, 2145–2148. [[CrossRef](#)]
14. Jegadeesan, R.; Nag, S.; Agarwal, K.; Thakor, N.V.; Guo, Y.X. Enabling Wireless powering and telemetry for peripheral nerve implants. *IEEE J. Biomed. Health Inform.* **2015**, *19*, 958–970. [[CrossRef](#)]
15. Wang, J.; Leach, M.; Lim, E.G.; Wang, Z.; Pei, R.; Huang, Y. An Implantable and Conformal Antenna for Wireless Capsule Endoscopy. *IEEE Antennas Wirel. Propag. Lett.* **2018**, *17*, 1153–1157. [[CrossRef](#)]
16. Jonah, O.; Georgakopoulos, S.V.; Tentzeris, M.M. Orientation insensitive power transfer by magnetic resonance for mobile devices. In Proceedings of the 2013 IEEE Wireless Power Transfer (WPT), Perugia, Italy, 15–16 May 2013; pp. 5–8.
17. Liu, D.; Hu, H.; Georgakopoulos, S. Misalignment Sensitivity of Strongly Coupled Wireless Power Transfer Systems. *IEEE Trans. Power Electron.* **2016**, *32*, 5509–5519. [[CrossRef](#)]
18. Jia, Y.; Mirbozorgi, S.A.; Wang, Z.; Hsu, C.C.; Madsen, T.E.; Rainnie, D.; Ghovanloo, M. Position and orientation insensitive wireless power transmission for enerCage-homecage system. *IEEE Trans. Biomed. Eng.* **2017**, *64*, 2439–2449. [[CrossRef](#)] [[PubMed](#)]
19. Lenaerts, B.; Puers, R. An inductive power link for a wireless endoscope. *Biosens. Bioelectron.* **2007**, *22*, 1390–1395. [[CrossRef](#)] [[PubMed](#)]
20. Zhiwei, J.; Guozheng, Y.; Jiangpingping; Zhiwu, W.; Hua, L. Efficiency optimization of wireless power transmission systems for active capsule endoscopes. *Physiol. Meas.* **2011**, *32*, 1561–1573. [[CrossRef](#)] [[PubMed](#)]
21. Bocan, K.N.; Mickle, M.H.; Sejdic, E. Multi-Disciplinary Challenges in Tissue Modeling for Wireless Electromagnetic Powering: A Review. *IEEE Sens. J.* **2017**, *17*, 6498–6509. [[CrossRef](#)]
22. Pacini, A.; Benassi, F.; Masotti, D.; Costanzo, A. Design of a RF-to-dc Link for in-body IR-WPT with a Capsule-shaped Rotation-insensitive Receiver. In Proceedings of the 2018 IEEE/MTT-S International Microwave Symposium-IMS, Philadelphia, PA, USA, 10–15 June 2018; pp. 1289–1292.

23. Khan, S.R.; Pavuluri, S.K.; Desmulliez, M.P.Y. New Analytical Model for the Characterisation of Printed Spiral Coils for Wireless Power Transfer. In Proceedings of the IEEE 12th European Conference on Antennas and Propagation (EuCAP), London, UK, 9–13 April 2018.
24. Theilmann, P.T.; Asbeck, P.M. An analytical model for inductively coupled implantable biomedical devices with ferrite rods. *IEEE Trans. Biomed. Circuits Syst.* **2009**, *3*, 43–52. [[CrossRef](#)] [[PubMed](#)]
25. Khan, S.R.; Pavuluri, S.K.; Desmulliez, M.P.Y. Accurate Modeling of Coil Inductance for Near-Field Wireless Power Transfer. *IEEE Trans. Microw. Theory Tech.* **2018**, *66*, 4158–4169. [[CrossRef](#)]
26. Kiani, M.; Jow, U.M.; Ghovanloo, M. Design and Optimization of a 3 Coil Inductive Link for Efficient Wireless Power Transmission. *IEEE Trans. Biomed. Circuits Syst.* **2011**, *5*, 579–591. [[CrossRef](#)]
27. Kiani, M.; Ghovanloo, M. A figure-of-merit for designing high-performance inductive power transmission links. *IEEE Trans. Ind. Electron.* **2013**, *60*, 5292–5305. [[CrossRef](#)]
28. Kim, J.; Park, Y.J. Approximate Closed-Form Formula for Calculating Ohmic Resistance in Coils of Parallel Round Wires with Unequal Pitches. *IEEE Trans. Ind. Electron.* **2015**, *62*, 3482–3489.
29. Wheeler, H.A. Formulas for the Skin Effect. *Proc. IRE* **1942**, *30*, 299–311. [[CrossRef](#)]
30. Kamidaki, C.; Guan, N. Theoretical Analysis of AC Resistance of Coil Made by Copper Clad Aluminum Wires. In Proceedings of the Progress in Electromagnetics Research Symposium Proceedings, Stockholm, Sweden, 12–15 August 2013; pp. 1730–1734.
31. Sullivan, C.R. Aluminum windings and other strategies for high-frequency magnetics design in an era of high copper and energy costs. *IEEE Trans. Power Electron.* **2008**, *23*, 2044–2051. [[CrossRef](#)]
32. Stratton, J.A. *Electromagnetic Theory*; Wiley: New York, NY, USA, 2007. (republishing of original 1941 McGraw-Hill edition).
33. Yang, Z.; Liu, W.; Basham, E. Inductor modeling in wireless links for implantable electronics. *IEEE Trans. Magn.* **2007**, *43*, 3851–3860. [[CrossRef](#)]
34. Kurs, A.; Karalis, A.; Moffatt, R.; Joannopoulos, J.D.; Fisher, P.; Soljacic, M. Wireless Power Transfer via Strongly Coupled Magnetic Resonances. *Science* **2007**, *317*, 83–86. [[CrossRef](#)] [[PubMed](#)]
35. Kiani, M.; Ghovanloo, M. The circuit theory behind coupled-mode magnetic resonance-based wireless power transmission. *IEEE Trans. Circuits Syst. I Regul. Pap.* **2012**, *59*, 2065–2074. [[CrossRef](#)] [[PubMed](#)]
36. Lay, H.; Cummins, G.; Cox, B.F.; Qiu, Y.; Turcanu, M.V.; McPhillips, R.; Connor, C.; Gregson, R.; Clutton, E.; Desmulliez, M.P.Y.; et al. In-Vivo Evaluation of Microultrasound and Thermometric Capsule Endoscopes. *IEEE Trans. Biomed. Eng.* **2018**, *66*, 632–639. [[CrossRef](#)]
37. Khan, S.R.; Pavuluri, S.K.; Cummins, G.; Desmulliez, M.P.Y. Miniaturized 3D Cross-Type Receiver for Wirelessly Powered Capsule Endoscopy. *IEEE Trans. Microw. Theory Tech.* **2019**, *67*, 1985–1993. [[CrossRef](#)]
38. Na, K.; Jang, H.; Ma, H.; Bien, F. Tracking optimal efficiency of magnetic resonance wireless power transfer system for biomedical capsule endoscopy. *IEEE Trans. Microw. Theory Tech.* **2015**, *63*, 295–303. [[CrossRef](#)]
39. Ding, K.; Yu, Y.; Lin, H.; Xie, J. Wireless Power Transfer at Sub-GHz frequency for Capsule Endoscope. *Prog. Electromagn. Res. C* **2016**, *66*, 55–61. [[CrossRef](#)]
40. Acar, M.; Annema, A.J.; Nauta, B. Generalized design equations for Class-E power amplifiers with finite DC feed inductance. In Proceedings of the 36th European Microwave Conference, Manchester, UK, 10–15 September 2006; pp. 1308–1311.
41. Liu, H.; Shao, Q.; Fang, X. Modeling and Optimization of Class-E Amplifier at Subnominal Condition in a Wireless Power Transfer System for Biomedical Implants. *IEEE Trans. Biomed. Circuits Syst.* **2017**, *11*, 35–43. [[CrossRef](#)]
42. Ping, S.; Hu, A.P. Analyses of DC Inductance Used in ICPT Power Pick-Ups for Maximum Power Transfer. In Proceedings of the 2005 IEEE/PES Transmission & Distribution Conference & Exposition: Asia and Pacific, Dalian, China, 18 August 2005; pp. 1–6.
43. Basar, M.R.; Yazed, M.; Cho, J.; Ibrahim, F. A Wireless Power Transmission System for Robotic Capsule Endoscopy: Design and Optimization. In Proceedings of the 2014 IEEE MTT-S International Microwave Workshop Series on RF and Wireless Technologies for Biomedical and Healthcare Applications (IMWS-Bio2014), London, UK, 8–10 December 2014; pp. 2–4.
44. Singeap, A.M.; Stanciu, C.; Trifan, A. Capsule endoscopy: The road ahead. *World J. Gastroenterol.* **2016**, *22*, 369–378. [[CrossRef](#)] [[PubMed](#)]

45. Khan, S.R.; Choi, G.S. High-efficiency CMOS rectifier with minimized leakage and threshold cancellation features for low power bio-implants. *Microelectron. J.* **2017**, *66*, 67–75. [[CrossRef](#)]
46. Mohamed, M.M.; Fahmy, G.A.; Abdel-Rahman, A.B.; Allam, A.; Barakat, A.; Abo-Zahhad, M.; Jia, H.; Pokharel, R.K. High-Efficiency CMOS RF-to-DC Rectifier Based on Dynamic Threshold Reduction Technique for Wireless Charging Applications. *IEEE Access* **2018**, *6*, 46826–46832. [[CrossRef](#)]



© 2019 by the authors. Licensee MDPI, Basel, Switzerland. This article is an open access article distributed under the terms and conditions of the Creative Commons Attribution (CC BY) license (<http://creativecommons.org/licenses/by/4.0/>).